IOP Publishing Nanotechnology
Nanotechnology 33 (2022) 065706 (8pp) https://doi.org/10.1088/1361-6528/ac34a7

Proton irradiation effects on mechanochemically synthesized and flash-evaporated hybrid organic–inorganic lead halide perovskites

Jiwon Shin[1], Kyeong-Yoon Baek[1], Jonghoon Lee[1], Woocheol Lee[1], Jaeyoung Kim[1], Juntae Jang[1], Jaehyoung Park[1], Keehoon Kang[2,*], Kyungjune Cho[3,*] and Takhee Lee[1]

[1] Department of Physics and Astronomy, and Institute of Applied Physics, Seoul National University, Seoul 08826, Republic of Korea
[2] Department of Materials Science & Engineering, Yonsei University, Seoul 03722, Republic of Korea
[3] Soft Hybrid Materials Research Center, Korea Institute of Science and Technology, Seoul 02792, Republic of Korea

E-mail: keehoon.kang@yonsei.ac.kr, kcho@kist.re.kr and tlee@snu.ac.kr

Received 20 September 2021, revised 25 October 2021
Accepted for publication 29 October 2021
Published 18 November 2021

Abstract

A hybrid organic–inorganic halide perovskite is a promising material for developing efficient solar cell devices, with potential applications in space science. In this study, we synthesized methylammonium lead iodide ($MAPbI_3$) perovskites via two methods: mechanochemical synthesis and flash evaporation. We irradiated these perovskites with highly energetic 10 MeV proton-beam doses of 10^{11}, 10^{12}, 10^{13}, and 4×10^{13} protons cm^{-2} and examined the proton irradiation effects on the physical properties of $MAPbI_3$ perovskites. The physical properties of the mechanochemically synthesized $MAPbI_3$ perovskites were not considerably affected after proton irradiation. However, the flash-evaporated $MAPbI_3$ perovskites showed a new peak in x-ray diffraction and an increased fluorescence lifetime in time-resolved photoluminescence under high-dose conditions, indicating considerable changes in their physical properties. This difference in behavior between $MAPbI_3$ perovskites synthesized via the abovementioned two methods may be attributed to differences in radiation hardness associated with the bonding strength of the constituents, particularly Pb–I bonds. Our study will help to understand the radiation effect of proton beams on organometallic halide perovskite materials.

Supplementary material for this article is available online

Keywords: mechanochemical synthesis, flash-evaporation, perovskite, proton irradiation, radiation hardness

(Some figures may appear in colour only in the online journal)

1. Introduction

Hybrid organic–inorganic halide perovskites have promising applications in optoelectronic and electronic devices, including solar cells, light-emitting diodes, lasers, photodetectors, and transistors [1–12], owing to their attractive properties, such as high power-conversion efficiency, large charge-carrier diffusion length, large absorption coefficient, and tunable direct bandgap [13, 14]. However, the stability of hybrid perovskites needs to be investigated under ambient and harsh environmental conditions

* Authors to whom correspondence should be addressed.

to demonstrate their practical applicability. In particular, given the prospect of high-efficiency perovskite solar cells being used in space environments, some researchers have studied the radiation tolerance of perovskite materials and devices to high-energy particles, such as cosmic rays, under space environments. For example, Lang *et al* investigated the radiation hardness of inverted methylammonium lead iodide ($MAPbI_3$) perovskite solar cells and found that these devices could tolerate 68 MeV proton-beam doses up to 10^{12} protons cm^{-2} [15]. Miyazawa *et al* found that lead halide perovskite solar cells could tolerate proton irradiation dose up to 10^{15} particles cm^{-2} with 50 keV proton beam which enable to implant proton particles within the perovskite layer causing lattice deformation [16]. However, the effect of isolating perovskites from the influences of other layers of the devices or interfaces that may affect the radiation hardness has not been adequately reported. Lang *et al* irradiated lead halide perovskite/copper indium gallium selenide (CIGS) and perovskite/silicon tandem solar cells and attributed most of the device efficiency losses to the CIGS and silicon layers and not the perovskite layer [17]. Therefore, exclusive research to investigate the apparent radiation hardness of the perovskite layer itself is necessary to avoid the influence of other surrounding layers.

In this study, we synthesized hybrid organic–inorganic $MAPbI_3$ perovskites via two methods: mechanochemical synthesis and flash evaporation. Then, we investigated the effects of irradiation on the physical properties of $MAPbI_3$ perovskites under various high-energy proton-beam doses. For this purpose, the physical properties of perovskites synthesized via two methods were characterized systematically before and after 10 MeV proton beam irradiation doses of 10^{11}, 10^{12}, 10^{13} and 4×10^{13} protons cm^{-2} using x-ray diffraction (XRD), ultraviolet–visible (UV–vis) absorbance spectroscopy, and photoluminescence. Mechanochemically synthesized $MAPbI_3$ perovskites did not exhibit considerable changes in their physical properties after the proton irradiations, indicating that this perovskite can tolerate dose conditions in this study. Conversely, flash-evaporated $MAPbI_3$ perovskites exhibited considerable changes in their physical properties after the high-dose proton irradiation. This study aims at broadening our understanding of the radiation tolerance of perovskite under high-energy proton-beam irradiation to estimate the potential of perovskites in space applications.

2. Experimental details

2.1. Mechanochemical synthesis of $MAPbI_3$ perovskite powder

$MAPbI_3$ perovskite powder was synthesized mechanochemically, as illustrated in figure 1. Figure 1(a) shows an optical image of the precursors 1.59 g methylammonium iodide (MAI) (white powder) and 4.61 g lead iodide (PbI_2) (yellow powder), ground using stainless steel balls with diameters of 1.27, 0.95, and 0.63 cm (4, 4, and 60 balls, respectively) in an alumina jar. The molecular structures of MAI and PbI_2 are schematically illustrated in figure 1(d). The alumina jar containing the mixture was ball milled at 300 Hz for 5 h (BD4530, LK Lab) (supplementary figure S1 (available online at stacks.iop.org/NANO/33/065706/mmedia)).

2.2. Synthesis of $MAPbI_3$ perovskite films via flash evaporation

As, previously reported, $MAPbI_3$ perovskite films were synthesized via a flash evaporation method [18, 19]. First, 500 μm thick glass substrates were cleaned via sonication in acetone, isopropyl alcohol, and deionized water for 10 min each. Then, the substrates were treated with O_2 plasma (30 sccm, 50 W) for 120 s using a reactive ion etcher (RIE; AFS-R4T, AllForSystem). These treated substrates were transferred to a vacuum chamber and placed in a substrate holder 30 cm above a source boat for flash evaporation (see figure 4(a)). To deposit $MAPbI_3$ perovskite film, we applied a high current of 100 A to rapidly heat the 650 mg mechanochemically synthesized $MAPbI_3$ powder and 167 mg MAI powder placed in the source boat to evaporate the source powder mixture.

2.3. Characterization of mechanochemically synthesized perovskite powder and flash evaporated perovskite film

The optical images and energy-dispersive spectra of the synthesized perovskite powder and film samples were acquired via field-emission scanning electron microscopy (FESEM; JSM-7800F Prime, JEOL Ltd). Powder or film XRD spectra were measured using an x-ray diffractometer (SmartLab, Rigaku) in the National Center for Interuniversity Research Facilities of Korea. Photoluminescence (PL) spectra and time-resolved (Tr) PL spectra were measured using the XperRAM 200 with a laser of 532 nm excitation wavelength and XperRF (Nanobase Inc.) with a pulsed laser that has a 405 nm excitation wavelength, 5000 kHz repetition rate, and 1 μW power, respectively. The absorbance spectra were acquired via UV–Vis spectroscopy (V-770, Jasco).

2.4. Proton irradiation

We used the MC-50 cyclotron at the Korea Institute of radiological and medical sciences for performing proton beam irradiation experiments. The 10 MeV proton beam irradiation source generated by 2×10^{10} protons per second per square centimeter, corresponding to a 10 nA average current had a ~1 cm spot size. Proton irradiation was performed in a vacuum environment. In order to irradiate the proton on the powder samples, the mechanochemically synthesized perovskite powder was placed on 15 μm thick Al foil. 140 mg perovskite powder was put on the Al foil with an area of 1.4 cm × 1.4 cm with a thickness of ~150 μm. The flash-evaporated perovskite film was directly attached to the equipment without any additional packing steps. The perovskite powder and films were irradiated at 10^{11}, 10^{12}, 10^{13}, and 4×10^{13} protons cm^{-2} proton-beam doses, which correspond to irradiation times of 5, 50, 500, and 2000 s, respectively. Cosmic ray proton flux varies depending on distance from earth, and the dose of 4×10^{13} protons cm^{-2} equivalent to the number of protons encountered in space over 10 years [20, 21]. To allow the radioactivity to fall to a safe level, the proton-

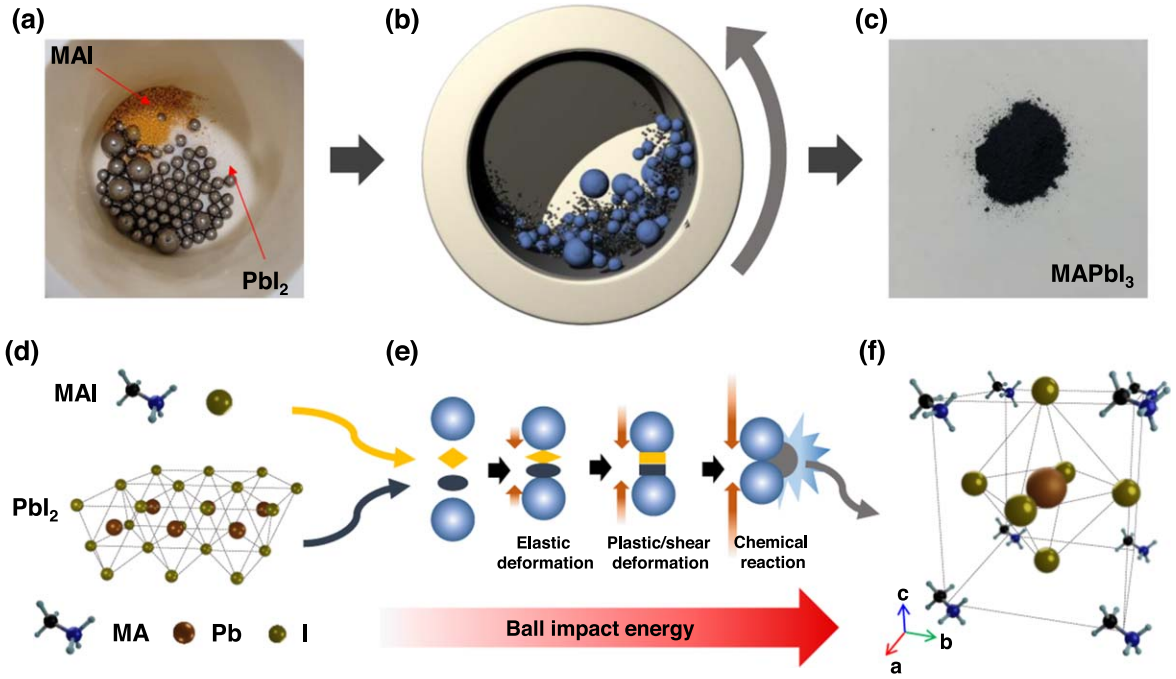

Figure 1. (a) Optical image of methylammonium iodide (MAI) and lead iodide (PbI_2) precursor powders in alumina jar. (b) Schematic of mechanochemical synthesis of $MAPbI_3$ perovskite through a ball mill. (c) Optical image of mechanochemically synthesized $MAPbI_3$ perovskite powder. (d) Structures of MAI and PbI_2 precursors. (e) Mechanism of mechanochemical reaction from reactants to products via soft ball milling. (f) Structure of $MAPbI_3$ perovskite unit cell.

irradiated samples were retained in the facility for one day after the completion of proton beam irradiation experiments.

3. Results and discussion

We used an electrically rotating ball mill in a so-called 'planetary instrument,' a simplified version of which is shown in figure 1(b), among various mechanochemical synthesis methods, such as hand-grinding or automated mixer mill methods. This method facilitates adequate controllability of rotation frequency and grinding force [22]. As the alumina jar rotates, mechanical energy, such as compression, shear, or friction, formed between the stainless balls or between the balls and the jar is transferred to the mixture (figures 1(b) and (e)). When sufficient energy is transferred, the chemical reaction occurs, and high-purity perovskite samples can be obtained as a form of dry colloidal powder. This method does not require dissolving reagents, and fresh-reactant surfaces are constantly exposed during the synthesis process [22–24]. Figure 1(c) presents an optical image that shows that the mechanochemically synthesized (denoted as 'MCS') $MAPbI_3$ perovskite powder is black as is known. Figure 1(f) shows the crystal structure of the MCS perovskite, which is the tetragonal phase. Note that flash-evaporated perovskite has the same tetragonal structure [25–27].

To verify whether MCS $MAPbI_3$ perovskite powder was well synthesized, we characterized its elemental composition and structural properties as well as photophysical properties using SEM, energy-dispersive x-ray spectroscopy (EDS), powder XRD, and PL. Figures 2(a) and (b) show the SEM images of the MCS $MAPbI_3$ perovskite powder with a particle size of tens to hundreds of nanometers. Uniform spatial distributions of elements such as C, Pb, and I were confirmed via EDS results (supplementary figure S2). The powder XRD peaks indicated that the MCS perovskite powder have a lattice structure of $MAPbI_3$ perovskite phase without remaining precursor PbI_2 that did not participate in the reaction (figure 2(c)) [28, 29]. Figure 2(d) shows a PL peak at ~770 nm from the steady-state PL emission with an excitation source of 532 nm, which corresponds to the known ~1.6 eV bandgap value of the MCS $MAPbI_3$ perovskite powder [28, 30]. Based on these experimental results, we confirmed that the MCS $MAPbI_3$ perovskite powder was successfully synthesized.

Then, the MCS $MAPbI_3$ perovskite powder was irradiated by 10 MeV proton beams under irradiation doses of 10^{11}, 10^{12}, 10^{13}, and 4×10^{13} protons cm^{-2}, respectively. We compared the physical properties of MCS $MAPbI_3$ perovskite powder systematically before and after proton irradiation to investigate the effects of proton irradiation. Figure 3(a) shows the XRD spectra of the MCS $MAPbI_3$ perovskite powder before proton irradiation (denoted as 'pristine') and after various proton irradiation doses. The XRD spectra did not indicate any considerable changes before and after proton irradiation, which suggests that the proton beam irradiation did not considerably affect the MCS $MAPbI_3$ perovskite powder. Furthermore, no conspicuous changes beyond the measurement error range were observed in the UV–vis absorbance (figure 3(b)) and PL results (figure 3(c)) of the MCS $MAPbI_3$ perovskite powder before and after proton irradiation although PL spectra seem to have slight variation in the peak width. Note that the PL spectra were the average values

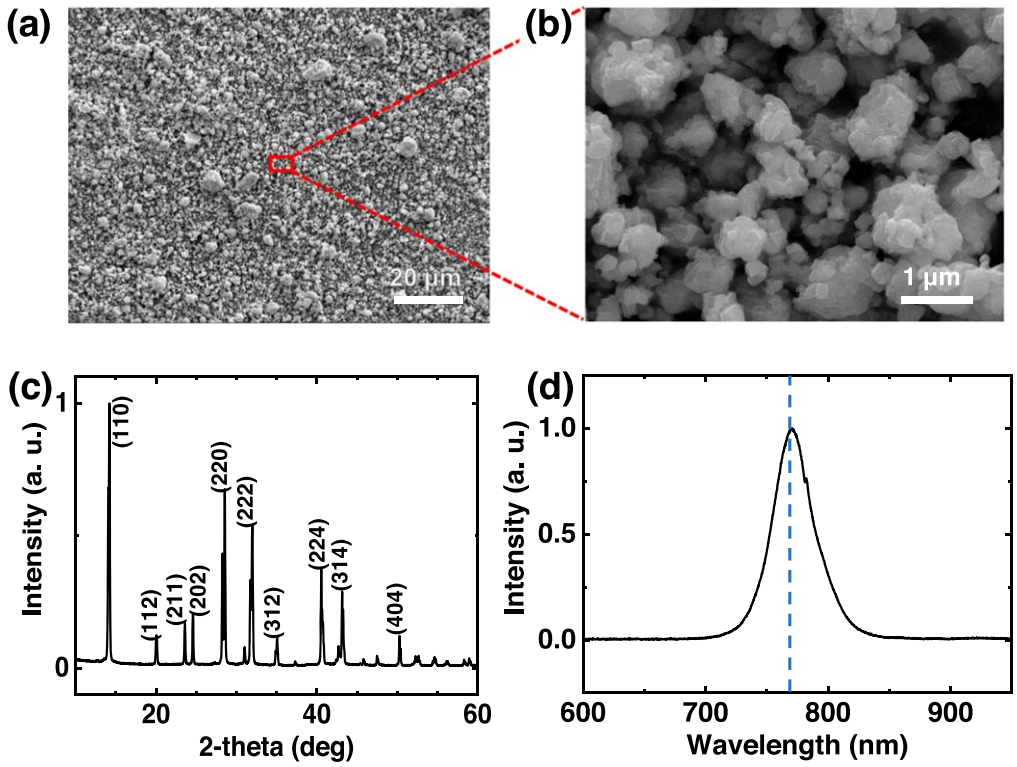

Figure 2. (a), (b) SEM images of MCS $MAPbI_3$ perovskite powder. (c) XRD spectrum of MCS $MAPbI_3$ perovskite powder. (d) Steady-state photoluminescence (PL) spectrum of MCS $MAPbI_3$ perovskite powder.

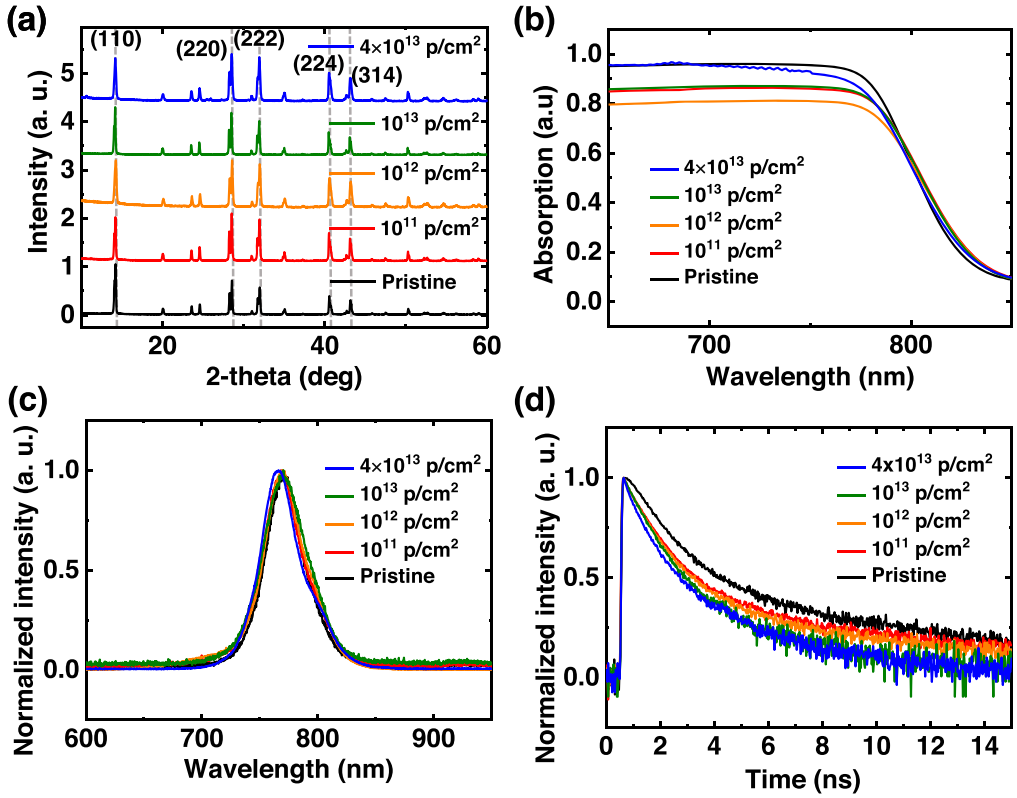

Figure 3. (a) XRD, (b) UV–vis absorbance, (c) PL, and (d) TRPL spectra of MCS $MAPbI_3$ perovskite powder samples before and after proton irradiation at doses of 10^{11}, 10^{12}, 10^{13}, and 4×10^{13} protons cm^{-2}.

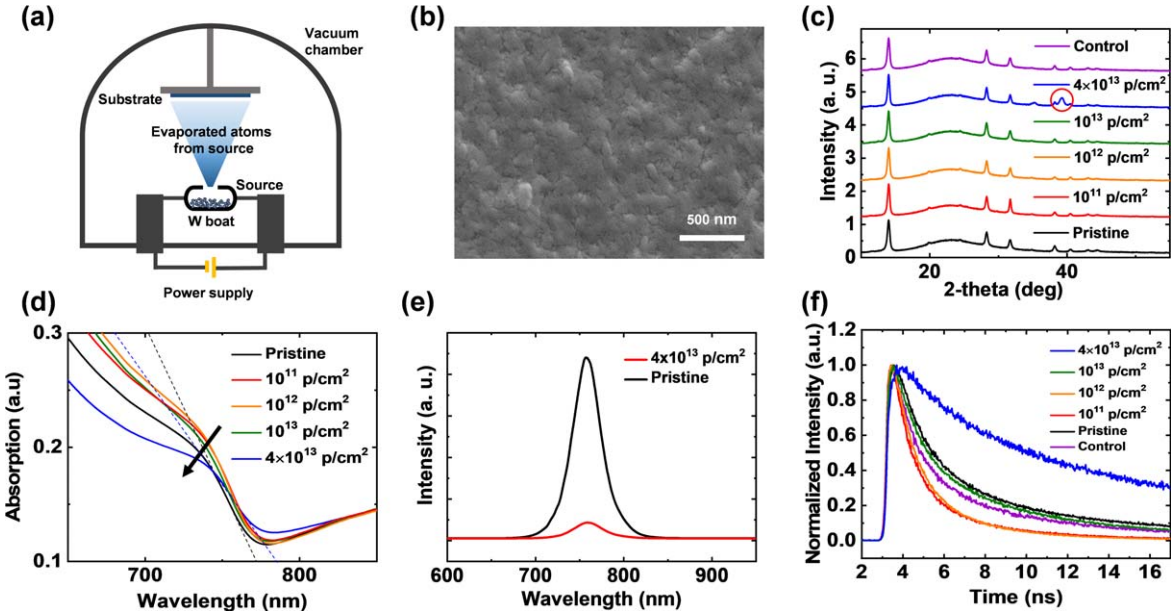

Figure 4. (a) Schematic of $MAPbI_3$ perovskite film deposition by flash evaporation. (b) SEM image of flash-evaporated $MAPbI_3$ perovskite film. (c) XRD, (d) UV–vis absorbance, (e) PL, and (f) TRPL spectra of flash-evaporated $MAPbI_3$ perovskite film samples before and after proton irradiation.

of point-scanned PL at four to five different positions and normalized because the intensity varies according to the location of the powder sample.

The MCS $MAPbI_3$ perovskite powder was also characterized by TRPL, which has proven to be a reliable and suitable tool for extracting minority-carrier lifetimes [31–33]. Figure 3(d) shows TRPL decay curves with excitation pulse laser of 405 nm wavelength and 5000 kHz repetition rate for the MCS $MAPbI_3$ perovskite powder. We analyzed these curves according to the following equation [34, 35]:

$$I(t) = a_1 e^{-t/\tau_1} + a_2 e^{-t/\tau_2} + b, \quad (1)$$

where a and τ are the amplitude and fluorescence lifetimes of the TRPL decay curve, respectively, and b is a fitting parameter. The subscripts 1 and 2 represent early- and late-stage recombination processes, respectively. The detailed fitting results are provided in the supplementary data (figures S3, S13(a) and table S1). Particularly, we found that both the τ_1 and τ_2 decreased with increasing irradiation dose. For the pristine case, τ_1 was found to be ~2.8 ns, which decreased from ~2.28 to ~2.02 ns for dose from 10^{11} to 4×10^{13} protons cm^{-2}. Similarly, τ_2 was found to be ~18.98 ns for the pristine case, which decreased from ~17.19 to ~7.27 ns for dose from 10^{11} to 4×10^{13} protons cm^{-2}. In other words, higher dose irradiation of the samples more accelerated the recombination process (i.e. τ values decreased). Overall, the results presented in figure 3 indicate that the proton irradiation did not cause considerable structural changes in the MCS $MAPbI_3$ perovskite powder (figures 3(a)–(c)); however, it accelerated the recombination process. This finding suggests that the proton beams might generate shallow traps that can allow trap-mediated recombination (figure 3(d)). A detailed discussion of this point is offered later. We also measured EDS after proton irradiation under dose of 4×10^{13} proton cm^{-2} (supplementary figure S4). In our results, no noticeable change in composition was observed between before and after proton irradiation on MCS perovskite powder, considering the measurement error range of the system.

We investigated the proton irradiation effect on flash-evaporated $MAPbI_3$ perovskite films. The flash evaporation process is schematically illustrated in figure 4(a). Detailed information regarding flash evaporation is provided in the experimental section. This flash evaporation method offers the advantages of rapid, solvent-free deposition for a large-scale production of organic–inorganic halide perovskite films [18, 36]. The flash-evaporated $MAPbI_3$ perovskite film in this study was ~150 nm-thick with a grain size of tens to hundreds of nanometers (figure 4(b) and supplementary figure S7). Similarly, the physical properties of flash-evaporated $MAPbI_3$ perovskite films were characterized using XRD, UV–vis absorbance, PL, and TRPL before and after proton irradiation. Figure 4(c) shows the XRD spectra of flash-evaporated perovskite film before and after proton irradiation. In this figure, the 'pristine' and 'control' curves represent the XRD spectra of the sample before proton irradiation, and that of the same pristine sample stored with other proton-irradiated samples under the same conditions, respectively. Note that all the samples were stored in a desiccator whose pressure was maintained at approximately 1 torr during travel between the laboratory and proton irradiation facility. Similar to the XRD spectra for the MCS $MAPbI_3$ perovskite powder (figures 2(c) and 3(a)), the XRD spectrum for the pristine $MAPbI_3$ perovskite film shows the peaks corresponding to the well-synthesized $MAPbI_3$ perovskite lattice structure (figure 4(c)), with broader XRD peak width than MCS powder, because the average grain size of flash-evaporated film (~17.12 nm) is smaller than MCS powder (~34.89 nm) which is obtained by the Scherrer equation [37]. It is noteworthy that the 2 theta

value for the peaks corresponding to the flash-evaporated $MAPbI_3$ perovskite film decreased by ~0.1° compared with those of the MCS $MAPbI_3$ perovskite powder samples (supplementary figure S9). This change may suggest that the MCS $MAPbI_3$ powder possesses a PbI_6 framework of superior compactness [25] with a less defective nature [38, 39] than that of the flash-evaporated $MAPbI_3$ film. The defect in iodide, which is significantly related to the stability of the perovskite, locally increases the electrostatic repulsion of lead cations in PbI_6 framework, thereby increasing the lattice size [25]. The broad peak around 25° can be attributed to the glass substrate. It is noteworthy that low dose (10^{11}, 10^{12}, and 10^{13} protons cm^{-2}) proton irradiation did not considerably affect the XRD spectra of the flash-evaporated $MAPbI_3$ perovskite films whereas high-dose (4×10^{13} protons cm^{-2}) proton irradiation produced a new peak around 39.2° (red circled in figure 4(c)), which indicates the presence of PbI_2 impurity generated via a high-dose proton irradiation in our samples [40].

Figures 4(d)–(f) show the UV–vis absorbance, PL, and TRPL data for the flash-evaporated perovskite films before and after the proton irradiation. As shown in figure 4(d), the absorbance onset position did not change much for all irradiation conditions, but the slope of the spectrum below ~750 nm became smaller after the proton irradiation of high-dose condition of 4×10^{13} proton cm^{-2}. Such change can also be associated with the slight deformation of $MAPbI_3$ which introduces additional trap sites in the bandgap, as previously reported [41]. The absorbance onset in the ~770 nm flash-evaporated $MAPbI_3$ perovskite films differed from that of the ~820 nm MCS $MAPbI_3$ perovskite powder samples (figures 3(b) and 4(d)). This disparity suggests smaller bandgap of MCS $MAPbI_3$ perovskite powders, which is associated with the less defects nature and superior compactness PbI_6 framework [25].

Figure 4(e) shows the PL data for the flash-evaporated $MAPbI_3$ perovskite film before (pristine) and after proton irradiation at the highest dose (4×10^{13} protons cm^{-2}). Note that the PL spectra of the flash-evaporated film are the average values of area scan (supplementary figure S10). The PL peak positions did not differ but the intensity decreased by approximately 90% after high-dose (4×10^{13} protons cm^{-2}) proton irradiation compared with that of the pristine sample. This can be attributed to the generated deep traps, which act as nonradiative recombination centers because the shallow traps such as Pb vacancies and MA interstitials, which are majority traps with the lowest defect formation energy in $MAPbI_3$ perovskite, do not act as non-radioactive recombination centers unlike deep defects [42, 43]. Notably, unlike the normalized PL spectra of the powder samples (figure 3(c)), the PL spectra of the flash-evaporated $MAPbI_3$ perovskite films are not normalized because the intensity does not vary according to the location of the uniform film sample. Thus, the intensity comparison is meaningful. The PL peak position for the ~760 nm flash-evaporated $MAPbI_3$ perovskite films differed slightly from that of the ~770 nm of the MCS $MAPbI_3$ perovskite powder samples (figures 3(c) and (e)). This disparity is consistent with the trend in absorbance data between the two sample types (figures 3(b) and 4(d)).

Figure 4(f) shows the TRPL data for the flash-evaporated $MAPbI_3$ perovskite films analyzed using equation (1). As the proton irradiation dose increased, the τ values were found to decrease relative to the pristine sample and then increase (supplementary figures S12, S13(b) and table S1). Particularly, τ_1 was ~1.91 ns for the pristine case, which decreased to ~1.04 ns at dose of 10^{11} protons cm^{-2} and increased from ~1.27 to ~4.71 ns at doses from 10^{12} to 4×10^{13} protons cm^{-2}, respectively. Similarly, τ_2 was ~11.23 ns for the pristine case, which decreased to ~4.59 and ~4.44 ns at doses of 10^{11} and 10^{12} protons cm^{-2} and increased to 7.63 and 20.44 ns at doses of 10^{13} and 4×10^{13} protons cm^{-2}, respectively. These results imply that the recombination process was accelerated when the samples were irradiated at low doses because of the generation of shallow traps. Conversely, the recombination process became slow when the samples were irradiated at high doses because of the generation of deep traps. Note that we obtained the coefficients of variations of fluorescence lifetime (supplementary table S2) to see the degree of variability. According to this, the variation in τ_2 is similar to that of τ_1. Also we conducted the EDS after proton irradiation for the flash-evaporated perovskite film under a dose of 4×10^{13} proton cm^{-2} (supplementary figure S5). Similar to the MCS perovskite sample, a noticeable change in composition after proton irradiation was not observed.

Figure 5(a) shows the energy-loss depth profiles of a 10 MeV proton beam based on the simulation results performed using stopping and range of ions in matter (SRIM) software, which is a computer program that calculates the interactions of energetic ions with target matter. There are two main processes in which a high-energy proton beam loses its energy. First, the high-energy protons are slowed down during the electronic stopping process, losing some energy and creating electron–hole pairs. Then, after the protons sufficiently slow down, they lose most of the energy during the nuclear stopping process and stop near the stopping depth, damaging the lattice of the target material [44–47]. Therefore, knowing the thickness of the target material compared with the stopping depth is necessary. According to the SRIM simulation results, as shown in figure 5(a), most protons have a stopping depth near 650 μm, which greatly exceeds the thickness of the perovskite samples (150 μm of MCS $MAPbI_3$ perovskite powder samples or 150 nm of flash-evaporated $MAPbI_3$ perovskite film samples). Most protons would pass through the samples while transferring energy via the ionization process in the material, creating homogeneous defects throughout the entire perovskite material (figure 5(b)).

When the proton beam irradiates perovskite, it can create electron–hole pairs along the irradiation path and break the bonds in the perovskite material. In this case, covalent bonds in the organic cation part (i.e. methylammonium, CH_3–NH_3^+), such as the C–H and N–H bonds, are vulnerable to protons because they have low bonding energy (left middle image of figure 5(c)). However, these broken-bond defects comprising mainly hydrogen vacancies in place of these bonds do not

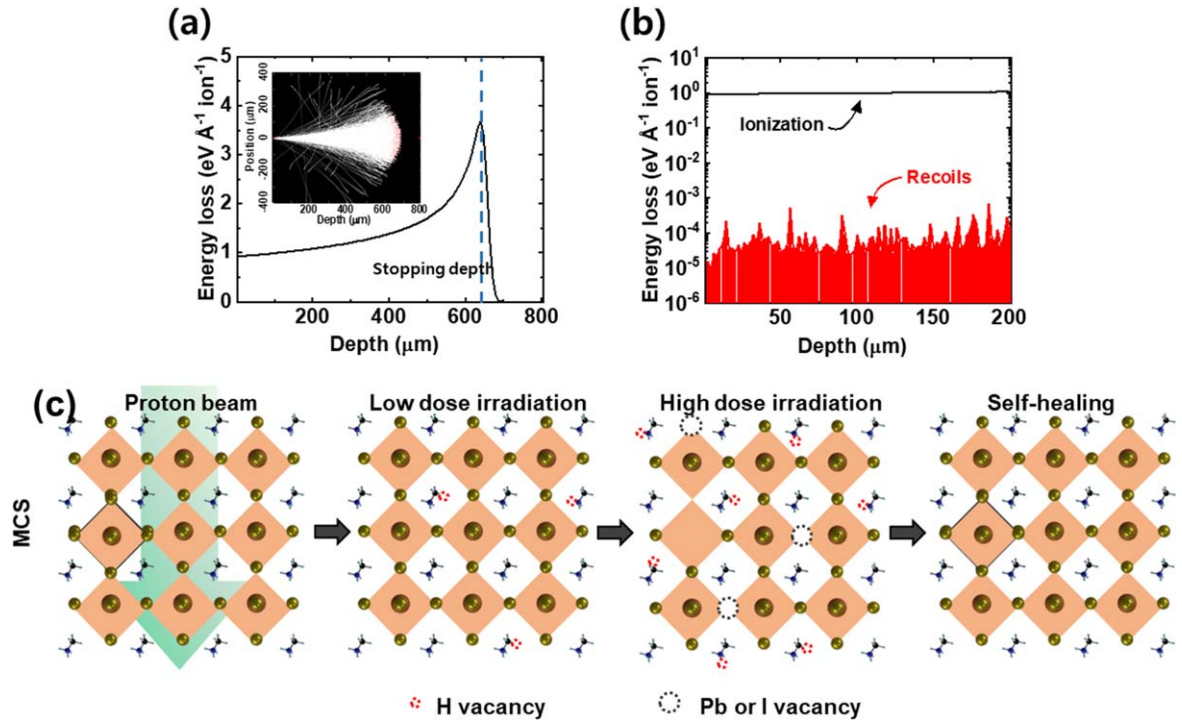

Figure 5. Energy loss profiles of protons simulated via SRIM (a) in the full range and (b) in the range of 0–200 μm. (c) Schematics depicting the effects of proton beam irradiation on perovskite. Left image shows schematic for pristine perovskite, two images in the middle show schematics for perovskite irradiated under a low dose (left middle), in which the effect of hydrogen vacancies is dominant, and a high-dose (right middle), in which the effects of lead and iodide vacancies increase. Right image shows schematic of self-healed perovskite in which hydrogen atoms released from bonds reassume their proper lattice positions.

significantly degrade the material, because the wandering hydrogen atoms that come off the bonds have high mobility so they can take the proper lattice position, which is called as 'self-healing' process (right image of figure 5(c)) [15, 48–51]. As the proton irradiation dose increases, constituent atoms of high bonding energy (i.e. Pb or I atoms in the PbI_6 framework) detach and remain as defects rather than relax back to their lattice positions (right middle image of figure 5(c)). The difference in radiation hardness between MCS $MAPbI_3$ perovskite powder and flash-evaporated $MAPbI_3$ perovskite film samples can be explained in terms of the bonding strength in the PbI_6 framework. As previously reported [25], the Pb–I bonds in MCS $MAPbI_3$ perovskite powder are stronger and shorter than those in flash-evaporated $MAPbI_3$ perovskite films. This difference is consistent with our results in terms of peak position differences obtained in XRD, PL, and UV–vis absorbance spectra (supplementary figure S9 for XRD, figure 3(c) versus figure 4(e) for PL, and figure 3(b) versus figure 4(d) for UV–vis absorbance).

4. Conclusion

We investigated the radiation hardness of organic–inorganic halide $MAPbI_3$ perovskites synthesized via mechanochemical synthesis and flash evaporation by measuring their physical and optical properties before and after the 10 MeV proton irradiation at various doses. The MCS $MAPbI_3$ perovskite powder samples did not exhibit considerable changes in their physical properties after the proton irradiation, indicating their radiation tolerance. Conversely, flash-evaporated $MAPbI_3$ perovskite film samples exhibited noticeable changes after irradiation at high doses. The radiation hardness difference between perovskite synthesis methods can be explained by the differences in the bonding strength of the PbI_6 frameworks in the irradiated perovskites. In particular, the Pb–I bonds in MCS $MAPbI_3$ perovskite powder are stronger than those in the flash-evaporated $MAPbI_3$ perovskite film. This study helps in expanding the scientific understanding of the radiation hardness of perovskite material and demonstrates the high radiation tolerance of MCS $MAPbI_3$ perovskite. Further study on an MCS $MAPbI_3$ perovskite powder that can be converted to a film without losing its properties will enhance the application potential of $MAPbI_3$ perovskite for devices in harsh radiative environments, such as space.

Acknowledgments

The authors appreciate the financial support of the National Research Foundation of Korea (NRF) grant (No. 2021R1A2C3004783, 2021R1C1C1010266, and 2021R1C1C2091728) and the Nano·Material Technology Development Program grant (No. 2021M3H4A1A02049651) through NRF funded by the Ministry of Science and ICT of Korea and the industry-university cooperation program by the Samsung Electronics Co., Ltd.

Data availability statement

All data that support the findings of this study are included within the article (and any supplementary files).

ORCID iDs

Takhee Lee https://orcid.org/0000-0001-5988-5219

References

[1] Mahmood K, Swain B S, Kirmani A R and Amassian A 2015 *J. Mater. Chem.* A **3** 9051
[2] Kim M, Kim G H, Oh K S, Jo Y, Yoon H, Kim K H, Lee H, Kim J Y and Kim D S 2017 *ACS Nano.* **11** 6057
[3] Niu T *et al* 2018 *Energy Environ. Sci.* **11** 3358
[4] Jeong J *et al* 2021 *Nature* **592** 381
[5] Tsai H *et al* 2018 *Adv. Mater.* **30** 1704217
[6] Zhao B *et al* 2018 *Nat. Photon.* **12** 783
[7] Stylianakis M M, Maksudov T, Panagiotopoulos A, Kakavelakis G and Petridis K 2019 *Materials* **12** 859
[8] Liu Y *et al* 2018 *Nat. Commun.* **9** 1
[9] Hwang B and Lee J S 2019 *Adv. Opt. Mater.* **7** 1801356
[10] Hwang B, Park Y and Lee J S 2021 *J. Mater. Chem.* C **9** 110
[11] Senanayak S P *et al* 2017 *Sci. Adv.* **3** e1601935
[12] Senanayak S P *et al* 2020 *Sci. Adv.* **6** eaaz4948
[13] McMeekin D P *et al* 2016 *Science* **351** 151
[14] Leveillee J, Katan C, Even J, Ghosh D, Nie W, Mohite A D, Tretiak S, Schleife A and Neukirch A J 2019 *Nano Lett.* **19** 8732
[15] Lang F *et al* 2016 *Adv. Mater.* **28** 8726
[16] Miyazawa Y, Ikegami M, Chen H W, Ohshima T, Imaizumi M, Hirose K and Miyasaka T 2018 *IScience* **2** 148
[17] Lang F *et al* 2020 *Joule* **4** 1054
[18] Lee J *et al* 2021 *Adv. Mater. Technol.* **6** 2001131
[19] Lee W *et al* 2020 *Sci Rep.* **10** 1
[20] Markvart T 1990 *J. Mater. Sci. Mater.* **1** 1
[21] Inguimbert C and Messenger S 2012 *IEEE Trans. Nucl. Sci.* **59** 3117
[22] Tan D and García F 2019 *Chem. Soc. Rev.* **48** 2274
[23] Palazon F, El Ajjouri Y and Bolink H J 2020 *Adv. Energy Mater.* **10** 1902499
[24] Elseman A, Shalan A, Rashad M and Hassan A 2017 *Mater. Sci. Semicond. Process.* **66** 176
[25] López C A *et al* 2020 *Sci. Rep.* **10** 1
[26] Jiang S *et al* 2016 *Angew. Chem.* **128** 6650
[27] Baikie T, Fang Y, Kadro J M, Schreyer M, Wei F, Mhaisalkar S G, Graetzel M and White T J 2013 *J. Mater. Chem.* A **1** 5628
[28] Kanaya S *et al* 2019 *J. Phys. Chem. Lett.* **10** 6990
[29] Guo X, McCleese C, Kolodziej C, Samia A C, Zhao Y and Burda C 2016 *Dalton Trans.* **45** 3806
[30] Caputo M *et al* 2019 *Sci. Rep.* **9** 1
[31] Ahrenkiel R 1992 *Solid-State Electron.* **35** 239–50
[32] Connelly B C, Metcalfe G D, Shen H and Wraback M 2010 *Appl. Phys. Lett.* **97** 251117
[33] Staub F, Hempel H, Hebig J C, Mock J, Paetzold U W, Rau U, Unold T and Kirchartz T 2016 *Phys. Rev. Appl.* **6** 044017
[34] Pham N D, Tiong V T, Chen P, Wang L, Wilson G J, Bell J and Wang H 2017 *J. Mater. Chem.* A **5** 5195
[35] James D R, Liu Y S, De Mayo P and Ware W R 1985 *Chem. Phys. Lett.* **120** 460
[36] Xu H *et al* 2016 *RSC Adv.* **6** 48851
[37] Muniz F T L, Miranda M A R, Morilla dos Santos C and Sasaki J M 2016 *Acta Crystallogr.* A **72** 385
[38] Prochowicz D, Franckevičius M, Cieślak A, Zakeeruddin S M, Grätzel M and Lewiński J 2015 *J. Mater. Chem.* A **3** 20772
[39] Jodlowski A D, Yépez A, Luque R, Camacho L and de Miguel G 2016 *Angew. Chem. Int. Ed.* **55** 14972
[40] Segovia R, Qu G, Peng M, Sun X, Shi H and Gao B 2018 *Nanoscale Res. Lett.* **13** 1
[41] Chaudhary B, Koh T M, Febriansyah B, Bruno A, Mathews N, Mhaisalkar S G and Soci C 2020 *Sci. Rep.* **10** 1
[42] Duan H S, Zhou H, Chen Q, Sun P, Luo S, Song T B, Bob B and Yang Y 2015 *Phys. Chem. Chem. Phys.* **17** 112
[43] Yin W J, Shi T and Yan Y 2014 *Appl. Phys. Lett.* **104** 063903
[44] Claeys C and Simoen E 2013 *Radiation Effects in Advanced Semiconductor Materials and Devices* (Berlin: Springer)
[45] Messenger S R, Burke E A, Summers G P, Xapsos M A, Walters R J, Jackson E M and Weaver B 1999 *IEEE Trans. Nucl. Sci.* **46** 1595–602
[46] Ziegler J F, Biersack J and Littmark U J 1985 *The Stopping and Range of Ions in Solids* (New York: Pergamon)
[47] Shin J *et al* 2019 *Nanoscale* **11** 13961
[48] Lang F, Shargaieva O, Brus V V, Neitzert H C, Rappich J and Nickel N H 2018 *Adv. Mater.* **30** 1702905
[49] Lang F, Jošt M, Bundesmann J, Denker A, Albrecht S, Landi G, Neitzert H C, Rappich J and Nickel N H 2019 *Energy Environ. Sci.* **12** 1634
[50] Brus V V *et al* 2017 *Adv. Electron. Mater.* **3** 1600438
[51] Malinkiewicz O, Imaizumi M, Sapkota S B, Ohshima T and Öz S 2020 *Emergent Mater.* **3** 9